

Diverse anisotropy of phonon transport in two-dimensional IV-VI compounds: A first-principles study

Guangzhao Qin,^{1,2} Zhenzhen Qin,³ Wu-Zhang Fang,⁴ Li-Chuan Zhang,¹
Sheng-Ying Yue,⁵ Qing-Bo Yan,^{1,*} Ming Hu,^{2,5,†} and Gang Su^{4,‡}

¹*College of Materials Science and Opto-Electronic Technology,
University of Chinese Academy of Sciences, Beijing 100049, China*

²*Institute of Mineral Engineering, Division of Materials Science and Engineering,
Faculty of Georesources and Materials Engineering,
RWTH Aachen University, Aachen 52064, Germany*

³*College of Electronic Information and Optical Engineering, Nankai University, Tianjin 300071, China*

⁴*School of Physics, University of Chinese Academy of Sciences, Beijing 100049, China*

⁵*Aachen Institute for Advanced Study in Computational Engineering Science (AICES),
RWTH Aachen University, Aachen 52062, Germany*

(Dated: December 9, 2024)

New class two-dimensional (2D) materials beyond graphene, including layered and non-layered, and their heterostructures, are currently attracting increasing interest due to their promising applications in nanoelectronics, optoelectronics and clean energy, where thermal transport property is one of the fundamental physical parameters. In this paper, we systematically investigated the phonon transport properties of 2D orthorhombic IV-VI compounds of *GeS*, *GeSe*, *SnS* and *SnSe* by solving the Boltzmann transport equation (BTE) based on first-principles calculations. Despite the similar puckered (hinge-like) structure along the armchair direction as phosphorene, the four monolayer compounds possess diverse anisotropic properties in many aspects, such as group velocity, Young's modulus and lattice thermal conductivity (κ), etc. Especially, the κ along the zigzag and armchair directions of monolayer *GeS* shows the strongest anisotropy while monolayer *SnS* and *SnSe* shows an almost isotropy in phonon transport, despite the similar characteristics of their structures. Based on the analysis of the frequency dependent κ and average phonon group velocity, we find that, the anisotropy mainly arises from the phonon modes below the gap in the phonon dispersions. The larger the gap, the stronger the anisotropy. This mechanism is explained from the coupling between the phonon modes on both sides of the gap and is further confirmed by the phonon scattering channels. We further show that the anisotropic behavior of the electron localization functions (ELF) reflecting the bonding characteristics is the physical origin of the anisotropic properties. Our study offers fundamental understanding of the anisotropic phonon transport properties of 2D compounds with hinge-like structure, and would be helpful for further modulation and applications in emerging technologies.

I. INTRODUCTION

The bulk orthorhombic IV-VI compounds of *GeS*, *GeSe*, *SnS* and *SnSe* possessing puckered (hinge-like) layered structure similar to black phosphorous have become a hot spot of recent researches.¹⁻⁶ The advantages of IV-VI compounds, such as earth-abundance, environmental compatibility, less toxicity, and chemical stability, make them very attractive for large-scale applications in photovoltaics and thermoelectrics.^{1,2,6-9} There have been a lot of studies on their optical properties including the photoconductivity, refractive index and infrared- and Raman-activity from experiments¹⁰⁻¹³ and first-principles calculations.^{14,15} The large thermopower, high power factors, and low thermal conductivities estimated using the Cahill's model¹⁶ make these four orthorhombic IV-VI compounds promising candidates for high-efficient thermoelectric materials.¹⁷ Bulk *SnSe* is especially a robust thermoelectric candidate for energy conversion applications in the low and moderate temperature range due to its anisotropic and low symmetry crystal structure.^{1,2}

The discovery of graphene leads to an upsurge in ex-

ploring two-dimensional (2D) materials, such as hexagonal boron nitride (*h*-BN), germanane, silicene, transition metal dichalcogenides (TMDCs) and phosphorene, which have attracted tremendous attention due to their unique dimension-dependent properties.¹⁸ In addition to the currently available 2D materials, 2D *SnSe* has been recently synthesized, which is greatly expected to be potential in the applications as photodetector, photovoltaic, piezoelectric and thermoelectric devices.¹⁹⁻²² Monolayer *SnSe* is also reported a promising 2D anisotropic semiconductor for nanomechanics, thermoelectrics, and optoelectronics,²³ and the quantum spin Hall effect was predicted in (111)-oriented thin films of *SnSe*.²⁴ Beyond the specific studies on 2D *SnSe*, there have also been a lot of studies on the optical properties of the four 2D orthorhombic IV-VI compounds of *GeS*, *GeSe*, *SnS* and *SnSe*.^{11,13,14} Furthermore, they are also reported as flexible, stable, and efficient 2D piezoelectric materials possessing enormous, anisotropic piezoelectric effects with the piezoelectric coefficients about two orders of magnitude larger than those of other 2D materials, such as *MoS₂*, *GaSe*, bulk *quartz* and *AlN*, which are widely used in industry.²¹ These novel 2D anisotropic

semiconductors, which attracted tremendous interest recently, have great potential applications in nanoelectronics, optoelectronics and thermoelectrics, calling for fundamental study of the phonon transport properties. However, the phonon transport properties of these 2D orthorhombic IV-VI compounds are still less known except monolayer *SnSe*.^{22,23} A complete and comparative prediction and understanding of the underlying phonon transport properties is the key to expand the range of their applications in nanoelectronics, optoelectronics and thermoelectrics.

In this paper, we conduct comprehensive investigations of the diverse phonon transport properties of 2D orthorhombic IV-VI compounds of *GeS*, *GeSe*, *SnS* and *SnSe* by solving the Boltzmann transport equation (BTE) based on first-principles calculations. The four monolayer compounds, although possessing similar hinge-like structure along the armchair direction as phosphorene, show diverse anisotropic properties in many aspects, such as group velocity, Young's modulus and lattice thermal conductivity (κ), etc. The remainder of the paper is organized as follows. In Sec. II, we briefly describe the methodology for the first-principles calculations and the Boltzmann transport theory of phonon transport. In Sec. III and IV, the optimized structures and phonon dispersions for the studied systems are presented, respectively. In Sec. V, we study the phonon transport properties of the four monolayer compounds with hinge-like orthorhombic structure. Furthermore, a detailed analysis on the diverse anisotropic properties is presented in Sec. VI from different aspects, including mode level κ and average group velocity, phonon scattering channels and electron localization function (ELF). In Sec. VII, the effect of finite size on κ and the anisotropy is studied. In Sec. VIII, we present the summary and conclusions.

II. METHODOLOGY

All the first-principles calculations are performed based on the density functional theory (DFT) using the projector augmented wave (PAW) method²⁵ as implemented in the Vienna *ab-initio* simulation package (VASP)²⁶. The Perdew-Burke-Ernzerhof (PBE)²⁷ of generalized gradient approximation (GGA) is chosen as the exchange-correlation functional. The kinetic energy cutoff of wave functions is 650 eV for *GeS* and *SnS*, and 550 eV for *GeSe* and *SnSe*, respectively, which are 2.5 times the maximal recommended cutoff in the pseudopotentials. A Monkhorst-Pack²⁸ k -mesh of $11 \times 11 \times 1$ is adopted to sample the Brillouin zone (BZ) of all the four monolayer compounds, with the energy convergence threshold set as 10^{-8} eV. In the supercell calculations for obtaining harmonic (second order) interatomic force constants (IFCs) and anharmonic (third order) IFCs, only Γ point in the reciprocal space is used for the purpose of saving resources.⁵ For 2D systems, a large vacuum spac-

ing is necessary to avoid the interactions between layers arising from the employed periodic boundary conditions. The vacuum spacing is set as at least 15 Å along the out-of-plane direction that is sufficiently large. Both the cell shape and volume are fully optimized and all atoms are allowed to relax until the maximal Hellmann-Feynman force acting on each atom is no larger than 0.001 eV/Å.

A sufficient large supercell is necessary for the accurate prediction of phonon dispersions, which is important for determining the phonon group velocities and phonon-phonon interactions that is critical for predicting thermal properties. In principle, the supercell should be constructed to ensure lattice constants at least larger than 10 Å. To determine the supercell size used in the real-space finite displacement difference calculations, we performed calculations with the supercell size of $2 \times 2 \times 1$, $3 \times 3 \times 1$, $4 \times 4 \times 1$ and $5 \times 5 \times 1$. The corresponding phonon dispersion curves show a convergent tendency as the supercell size increasing, such as the coupling among optical and acoustic phonon branches, the smoothness of the phonon dispersion curves, the shift of frequencies of phonon modes at Γ -point, and the flat dispersions near the S symmetry point. Since there is no difference between the results obtained with the supercell size of $4 \times 4 \times 1$ and $5 \times 5 \times 1$, it is doubtless that the supercell size of $5 \times 5 \times 1$ is a good choice.

The force constant $C_{i\alpha;j\beta}$ can be obtained from the force caused by displacement:

$$C_{i\alpha;j\beta} = -\frac{F_{i\alpha}}{\Delta_{j\beta}}, \quad (1)$$

where $F_{i\alpha}$ is the force along the α direction acting on atom i resulted from the displacement along the β direction of atom j ($\Delta_{j\beta}$). The displacement amplitude of atom along the $\pm x$, $\pm y$ and $\pm z$ directions are 0.01 Å. The space group symmetry properties are used to reduce the calculation cost and numerical noise of the force constants, and it can also greatly simplify the determination of the dynamical matrix that is constructed based on the force constants. The frequency and eigenvector forming the phonon dispersions can be obtained by diagonalizing the dynamical matrix.

Besides the harmonic IFCs obtained above, anharmonic IFCs, which are used for the determination of the scattering properties, are also necessary in the calculation of lattice thermal conductivity (κ). A $4 \times 4 \times 1$ supercell is constructed to get the anharmonic IFCs, and the first-principles based real-space finite displacement difference approach is employed. A cutoff radius (r_{cutoff}) is introduced to discard the interactions between atoms with distance larger than a certain value for practical purposes. In principle, the r_{cutoff} should exceed the range of physically relevant anharmonic interactions to get satisfactory results.^{29,30} Here, referring to the converged cutoff radius as examined in the previous work, we choose a cutoff radius of about 6.5 Å, which includes up to 15-*th*, 14-*th*, 13-*th* and 11-*th* nearest neighbors for *GeS*, *GeSe*, *SnS* and *SnSe*, respectively.⁵ The dielectric tensor and Born

effective charges are also obtained to take into account of long-range electrostatic interactions. We choose the thickness of monolayer as half the length of the lattice constant along the out-of-plane direction of the layered bulk counterpart, which contains two layers in the conventional cell.³¹ The specific values of the thickness of the four monolayer compounds are listed in Table I.

The lattice thermal conductivity (κ) is calculated by solving the linearized BTE for phonons. At thermal equilibrium, the phonons are distributed obeying the Bose-Einstein function $f_0(\omega_\lambda)$ in the absence of temperature gradient or other thermodynamical forces. The λ is the index of phonon mode comprising both phonon polarization p and wave vector \mathbf{q} . The ω_λ is the angular frequency. In the steady state with a temperature gradient ∇T , the phonon distribution function f_λ deviates from $f_0(\omega_\lambda)$ and this deviation can be obtained from the BTE:

$$\frac{\partial f_\lambda}{\partial t} = \nabla T \cdot \mathbf{v}_\lambda \frac{\partial f_\lambda}{\partial T}, \quad (2)$$

where \mathbf{v}_λ is the group velocity. The left side is the scattering term that can be determined by taking into account the anharmonic scattering due to intrinsic phonon-phonon interactions and the harmonic scattering due to defects and impurities such as isotopes. The right side is the diffusion term caused by the temperature gradient ∇T . Assuming a small enough ∇T in most practical situations, Eq. (2) can be linearized in ∇T and re-written as:

$$f_\lambda - f_0(\omega_\lambda) = -\mathbf{F}_\lambda \cdot \nabla T \frac{df_0}{dT}, \quad (3)$$

where $\mathbf{F}_\lambda = \tau_\lambda^0(\mathbf{v}_\lambda + \mathbf{\Delta}_\lambda)$ when only considering the scattering mechanism of two- and three-phonon processes. Here, τ_λ^0 is the relaxation time obtained from perturbation theory, which is commonly used within the relaxation time approximation (RTA), and $\mathbf{\Delta}_\lambda$ in the dimension of velocity is a correction of the deviation to the RTA prediction. The τ_λ^0 can be computed as:

$$\frac{1}{\tau_\lambda^0} = \frac{1}{N} \left(\sum_{\lambda'\lambda''}^+ \Gamma_{\lambda\lambda'\lambda''}^+ + \sum_{\lambda'\lambda''}^- \frac{1}{2} \Gamma_{\lambda\lambda'\lambda''}^- + \sum_{\lambda'} \Gamma_{\lambda\lambda'} \right), \quad (4)$$

where $N = N_1 \times N_2 \times N_3$ is the number of discrete \mathbf{q} sampling in the BZ, which should be tested for the convergence of κ , and $\Gamma_{\lambda\lambda'\lambda''}^+$ and $\Gamma_{\lambda\lambda'\lambda''}^-$ are three-phonon scattering rates corresponding to absorption and emission processes of phonons, respectively, and $\Gamma_{\lambda\lambda'}$ is the scattering possibility resulted from the disorder of isotopic impurity.

Eq. (3) is numerically solved by iterating from a zeroth order approximation start of $\mathbf{F}_\lambda = \tau_\lambda^0 \mathbf{v}_\lambda$. If the iteration stops at the first step, the procedure is equivalent to the operation in the RTA. The iterative procedure has a large impact on the study of materials such as diamond in which the normal processes play a significant role in the phonon-phonon scattering.³² In such situations, the RTA

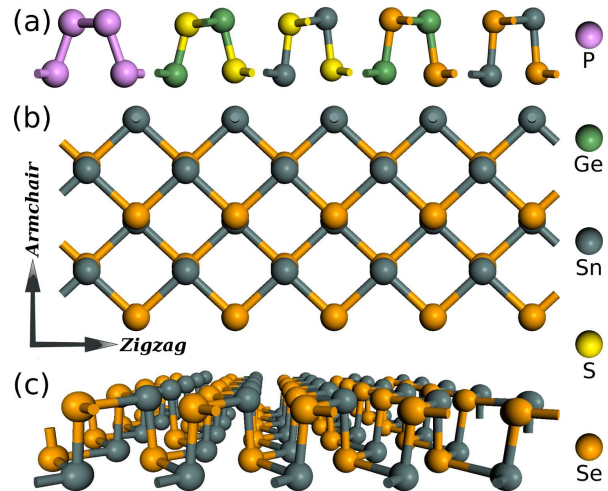


FIG. 1. (Color online) (a) From left to right: side view of the monolayer of black phosphorus, *GeS*, *SnS*, *GeSe* and *SnSe*. (b) Top view of monolayer *SnSe*. The zigzag and armchair directions are indicated with arrows. (c) Perspective view of monolayer *SnSe*. The species of atoms are shown on the right.

treating the normal process resistive cannot yield reasonable results. In contrast, in materials such as Si and Ge with strong Umklapp scattering, iterating to convergence only leads to a less than 10% increase of the room temperature κ compared to the RTA result.³³ Based on the solution, the heat flux can be calculated and the κ can be obtained in terms of \mathbf{F}_λ :

$$\kappa^{\alpha\beta} = \frac{1}{k_B T^2 N \Omega} \sum_{\lambda} f_0(f_0 + 1) (\hbar \omega_\lambda)^2 v_\lambda^\alpha F_\lambda^\beta \quad (5)$$

where k_B is the Boltzmann constant, \hbar is the Planck constant, Ω is the volume of the unit cell, and α and β denote the Cartesian components in the conventional cubic unit cell. The approach described above yields predictive parameter free estimate of κ using only basic information of the chemical structure, and has been implemented in the **SHENGBTE** code^{30,34} as employed in this work.

III. STRUCTURES

The cell shape, volume and atoms are fully relaxed till convergence reached. Along with the monolayer of black phosphorus that is called phosphorene, the optimized structures of monolayer *GeS*, *SnS*, *GeSe* and *SnSe* are shown in Fig. 1(a) from left to right. All these monolayer materials belong to the same orthorhombic crystal system, and possess similar hinge-like structure along the armchair direction, which is a typical feature distinctly different from the flat graphene and buckled silicene. As reviewed in previous work, the hinge-like structure will introduce strong anisotropic properties.^{35,36} For example, it is harder along the zigzag direction than that along the armchair direction, which can be verified by the Young's

modulus. The hinge-like orthorhombic structure generally leads to the lattice constants being larger along armchair direction than along zigzag direction. The obtained lattice constants along the two lattice directions are different, as listed in Table I. The difference from large to small is monolayer $GeS > GeSe > SnS > SnSe$. Compared with monolayer GeS and $GeSe$, the difference of lattice constants along the two directions for monolayer SnS and $SnSe$ are very small, leading to their symmetric square-like lattice structures. This symmetric square-like lattice structure may have significant influence on the atomic bonding along the two directions, and will lead to their less anisotropic properties, as we will see later.

All the space groups of the four monolayer compounds are the same $Pmn2_1$ (No. 31), possessing 4 symmetry operators, which is different from that of phosphorene ($Pmna$ (No. 53), possessing 8 symmetry operators). The lower symmetry of the four monolayer compounds compared with phosphorene lies in the different types of atoms constituting the compounds, in which the two sublayers are not parallel to each other. It is interesting to note from Fig. 1(a) that the metallic atoms Ge interpose between the non-metallic (metalloid) atoms Se along the out-of-plane direction in monolayer $GeSe$, which is different from that in monolayer GeS , SnS and $SnSe$ where the non-metallic atoms interpose between the metallic atoms along the out-of-plane direction. The difference may be due to the same period of Ge and Se in the periodic table resulting in the closest mass of the two atoms and the smallest electronegativity difference in the binary compound.

IV. PHONON DISPERSIONS

In the calculation of phonon dispersions, a $5 \times 5 \times 1$ supercell containing 100 atoms is constructed and the first-principles based finite displacement difference method is employed.^{37,38} As shown in Fig. 2, the phonon dispersions of monolayer GeS , SnS , $GeSe$ and $SnSe$ have no imaginary part, indicating the thermodynamic stability of the four monolayer compounds. There exist 3 acoustic and 9 optical, that is 12 in total, phonon branches corresponding to the 4 atoms per unit cell. The three lowest phonon branches are acoustic phonon branches, i.e. the out-of-plane flexural acoustic (FA) mode, the in-plane transverse acoustic (TA) mode and the in-plane longitudinal acoustic (LA) mode. The TA and LA branches is linear near the Γ point while the FA branch is flexural, which is similar to other 2D materials such as graphene, silicene, and phosphorene.^{36,39-42} This flexural feature is typically due to the 2D nature of monolayer structure.⁴⁰

The four monolayer compounds show very similar dispersion curves along the path passing through the main high-symmetry k -points in the irreducible Brillouin zone (IBZ) except: 1) The phonon dispersions of monolayer GeS and $GeSe$ are separated into two regions with each region possessing 6 branches. There exists a gap be-

tween the two regions. The gap is 2.014 THz for monolayer GeS and 0.105 THz for monolayer $GeSe$. However, there is no similar gap for monolayer SnS and $SnSe$. 2) The phonon dispersions of SnS and $SnSe$ are characterized by markedly dispersive optical phonon branches, which lead to the disappearance of the gap and result in significant group velocities of optical phonon branches. 3) The frequencies of the four monolayer compounds are different, especially the maximum frequency (ω_M) of optical phonon branches at Γ point, and the order of ω_M is monolayer $GeS > SnS > GeSe > SnSe$. This may be owing to the different reduced atomic mass ($\mu = m_1 m_2 / (m_1 + m_2)$) that the larger the μ the lower the maximum frequency. The order of μ of the four monolayer compounds is $GeS < SnS < GeSe < SnSe$ that is opposite to the order of ω_M .

From the overview of Fig. 2, it is obvious that monolayer SnS and $SnSe$ possess almost symmetric phonon dispersion curves along the Γ -X-S (left) and Γ -Y-S (right) high-symmetry k -paths, while the symmetry for monolayer GeS is most broken, especially for the low-frequency phonon modes. As a result, the anisotropy of group velocity along the two different directions of monolayer SnS and $SnSe$ is tiny, and that of monolayer GeS and $GeSe$ is much larger. Based on the slope of the LA branch near the Γ point, we could get the group velocities along Γ -X (zigzag) and Γ -Y (armchair) directions, respectively. As listed in Table I, the specific values of the group velocities of the four monolayer compounds show different anisotropy along the zigzag and armchair directions. The anisotropy of group velocities along the two directions from large to small is monolayer $GeS > GeSe > SnS > SnSe$. From the lattice constants as listed in Table I, it is found that the order of anisotropy of group velocities is the same as that of lattice constants. It is reviewed in previous work that the hinge-like structure of phosphorene is the key to the strong anisotropy of its properties.^{35,36} However, monolayer $SnSe$ shows an almost isotropic behavior despite its similar hinge-like structure as phosphorene. The reason may lie in the symmetric square-like lattice structure²³ and the large atomic mass of Sn and Se , which counteract the anisotropy introduced by its hinge-like structure.

V. PHONON TRANSPORT PROPERTIES

Based on the harmonic and anharmonic IFCs, the lattice thermal conductivity (κ) is calculated by solving the linearized BTE for phonons. The phonon Q -grid sampling ($N \times N$) in the BZ as shown in Eq. (4) has been fully tested for the convergence of κ . The N of 46, 68, 47 and 48 is chosen for getting the convergent κ of monolayer GeS , $GeSe$, SnS and $SnSe$, respectively. By employing the iterative method, the obtained κ along zigzag and armchair directions of the four monolayer compounds at different temperatures are collected together for comparison, as shown in Fig. 3. The specific values of κ at 300 K

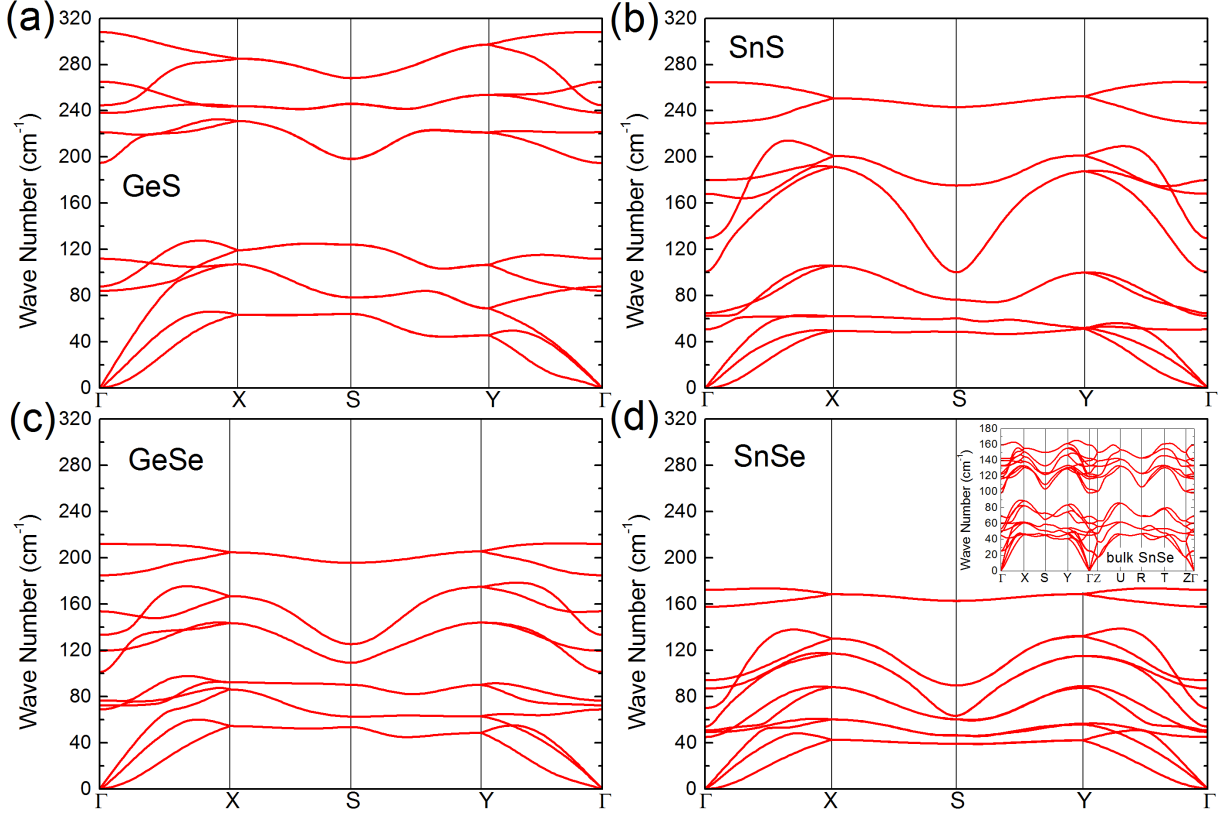


FIG. 2. (Color online) The phonon dispersion curves along the path passing through the main high-symmetry k -points in the irreducible Brillouin zone of monolayer (a) GeS , (b) SnS , (c) $GeSe$ and (d) $SnSe$. The phonon dispersion curves of bulk $SnSe$ is shown in the inset of (d) for comparison. The Γ -X and Γ -Y correspond to the zigzag and armchair directions, respectively.

TABLE I. Lattice constants, thickness, Young's modulus (E), group velocity (v_g) at Γ point, lattice thermal conductivity (κ) at 300 K, the parameter α in the relation of $\kappa \sim 1/T^\alpha$, the percentage contribution to κ of acoustic phonon branches (FA, TA and LA) and optical phonon branches at 300 K and the representative mean free path (rMFP) at 300 K. The thickness of monolayer is chosen as half the length of the lattice constant along z direction of the bulk counterpart. The properties of bulk $SnSe$ are also listed in addition to the four monolayer compounds of GeS , $GeSe$, SnS and $SnSe$.

Structure	Direction	Lattice constant (Å)	Thickness (Å)	E (GPa)	v_g (km/s)	κ ($Wm^{-1}K^{-1}$)	α	Contribution (%)				rMFP (nm)
								FA	TA	LA	optical	
GeS	zigzag	3.671	5.361	29.74	4.21	9.81	1.019	35.07	24.52	28.01	12.40	24.44
	armchair	4.457		7.80	2.66	2.94	0.986	25.90	26.88	26.38	20.84	15.23
$GeSe$	zigzag	3.982	5.561	54.63	3.59	5.89	0.997	29.41	25.18	28.45	16.96	23.30
	armchair	4.269		22.10	2.73	4.57	0.996	37.47	26.47	20.61	15.45	72.51
SnS	zigzag	4.088	5.714	44.11	3.37	3.21	0.990	27.07	19.79	25.97	27.17	13.07
	armchair	4.265		25.30	2.94	2.95	0.984	34.18	17.67	18.84	29.31	13.25
$SnSe$	zigzag	4.294	5.888	45.14	3.13	2.95	0.999	31.39	25.16	14.90	28.55	12.04
	armchair	4.370		23.72	2.97	2.59	0.998	30.13	23.21	16.40	30.26	10.44
bulk $SnSe$	zigzag	4.214	11.776	42.21	3.08	1.77	0.971	17.66	10.20	9.21	62.93	6.86
	armchair	4.520		21.16	2.51	0.84	0.946	10.96	13.21	8.86	66.97	4.30

are listed in Table I. We also calculated the κ by using the RTA method, and found that iterating to convergence will lead to monolayer GeS : (36.5%, 22.3%), $GeSe$: (13.9%, 8.7%), SnS : (15.8%, 16.5%) and $SnSe$: (11.6%, 11.3%) increase of the room temperature κ compared to the RTA results, which means stronger Umklapp scattering existing in monolayer $GeSe$, SnS and $SnSe$ than

monolayer GeS . The two numbers in the parentheses are the ratio of increase for zigzag and armchair directions, respectively. The calculated κ at different temperatures as shown in Fig. 3(a) decrease with temperature increasing. By fitting with the relation of $\kappa \sim 1/T^\alpha$, the parameter α are almost equal to 1, as listed in Table I, which is consistent with the common behavior of κ at medium

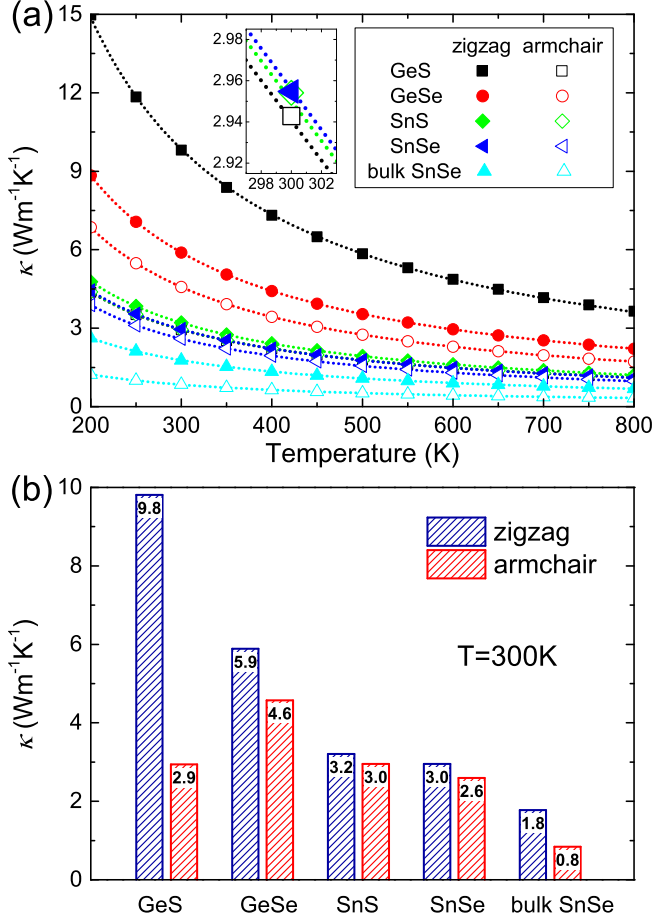


FIG. 3. (Color online) The lattice thermal conductivity (κ) of monolayer *GeS*, *GeSe*, *SnS* and *SnSe* along zigzag and armchair directions. The in-plane κ of bulk *SnSe* are also plotted for comparison. (a) κ as a function of temperature ranging from 200 K to 800 K. The dot lines show the fitting result of $\kappa \sim 1/T^\alpha$. The very close κ along the zigzag direction of monolayer *SnSe* and along the armchair direction of monolayer *GeS* and *SnS* are amplified as clearly shown in the insert. (b) Anisotropic κ along zigzag and armchair directions at 300 K for the four monolayer compounds and bulk *SnSe*.

temperatures for semi-conductors.^{36,43,44}

The average κ along the two directions of the four monolayer compounds and bulk *SnSe* are *GeS* (6.38 Wm⁻¹K⁻¹), *GeSe* (5.23 Wm⁻¹K⁻¹), *SnS* (3.08 Wm⁻¹K⁻¹), *SnSe* (2.77 Wm⁻¹K⁻¹) and bulk *SnSe* (1.31 Wm⁻¹K⁻¹), respectively. They possess the rather low thermal conductivity compared to a lot of materials, such as *h*-BN, MoS₂, graphene, silicene, phosphorene, etc.^{36,41,45,46} The κ is strongly affected by the scattering processes, which can be influenced by the anharmonic nature of structure and the number of allowed three-phonon scattering processes, which are quantified as the Grüneisen parameters (γ) and anharmonic phase space volume (P_3), respectively.⁵ The order of κ is monolayer *GeS* > *GeSe* > *SnS* > *SnSe* > bulk *SnSe*, which is consistent with the order of P_3 as shown in Fig. 4(c)

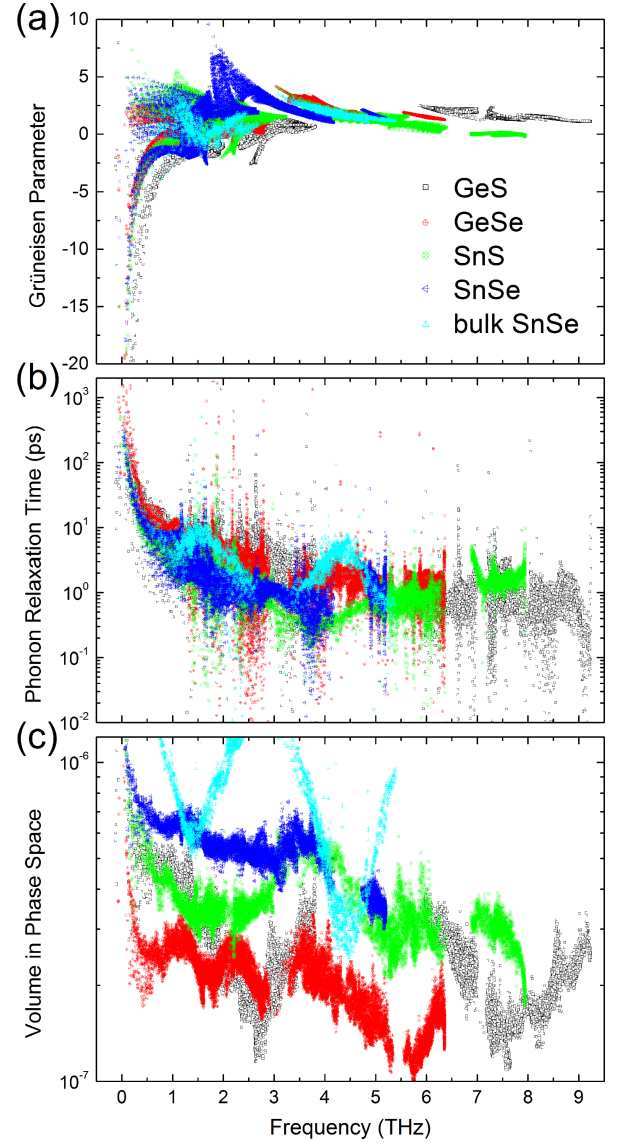


FIG. 4. (Color online) (a) Grüneisen parameter (γ), (b) phonon relaxation time (τ) and (c) volume in phase space (P_3) as a function of frequency at 300 K of monolayer *GeS* (black), *GeSe* (red), *SnS* (green) and *SnSe* (blue) and bulk *SnSe* (cyan).

except monolayer *GeS*. Though monolayer *GeS* has the largest κ , it does not possess a smallest P_3 . However, its γ at low frequency range is obviously much smaller than the other monolayer compounds. The anharmonic nature of monolayer *GeS* is weak compared to the other monolayer compounds, resulting in its largest κ . The largest κ of monolayer *GeS* could also be understood from its phonon dispersion. As compared in Sec. IV, the phonon dispersion of monolayer *GeS* possess the largest gap of 2.014 THz (Fig. 2(a)), which is much larger than that of monolayer *GeSe* (0.105 THz), while monolayer *SnS* and *SnSe* have no gap. The large phonon energy gap causes that the scattering of acoustic phonon modes due to the optical phonon modes is much weaker⁴⁷, which leads to

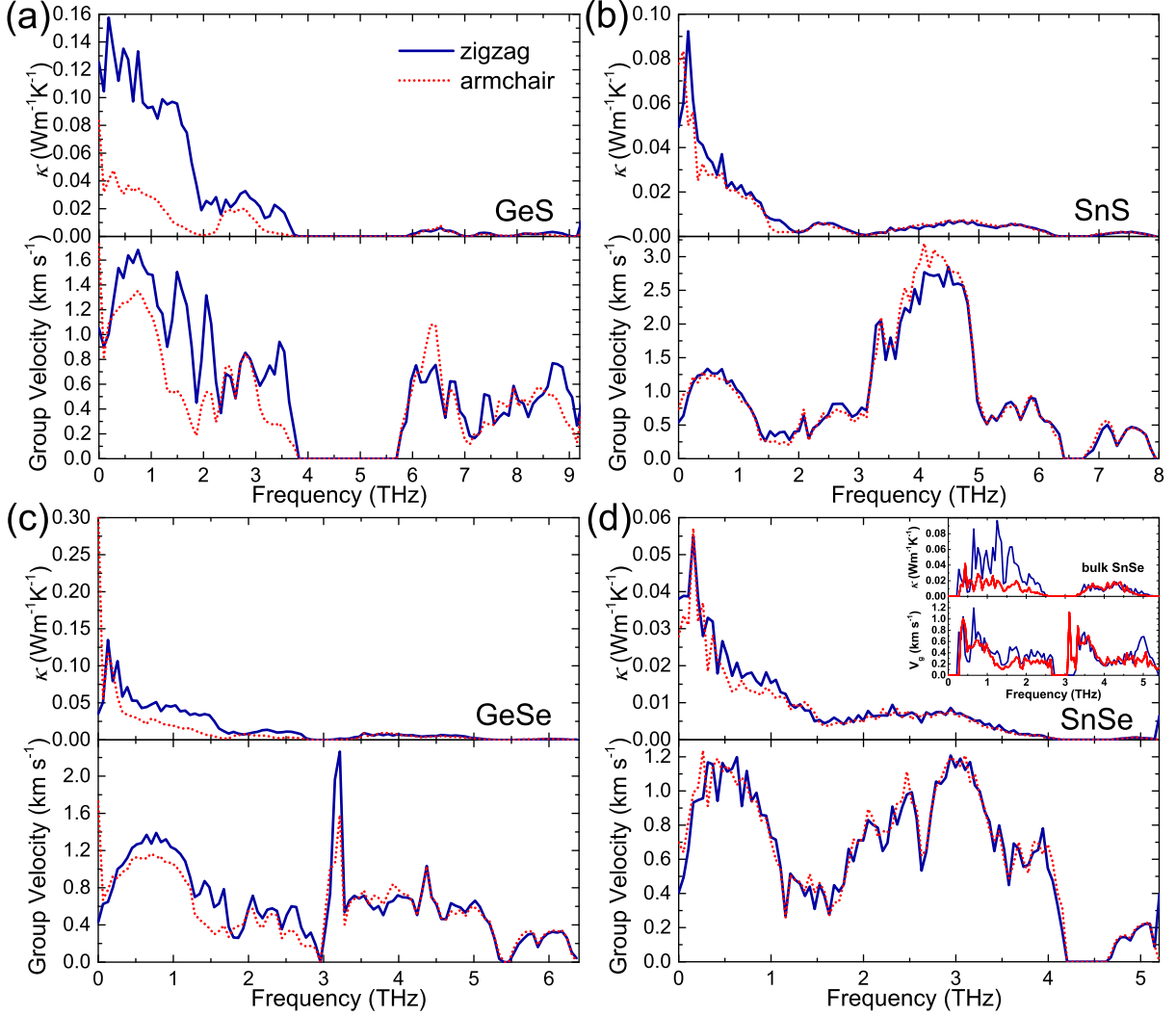


FIG. 5. (Color online) The frequency dependent lattice thermal conductivity (κ) and average group velocity (V_g) of monolayer (a) *GeS*, (b) *SnS*, (c) *GeSe* and (d) *SnSe* along zigzag and armchair directions. The κ and V_g are summed up and averaged for all the phonon modes in each small frequency bins, respectively. The corresponding values of bulk *SnSe* are shown in the inset of (d) for comparison.

the higher κ of monolayer *GeS*. Though there is a big gap in the phonon dispersion of bulk *SnSe* as well, the κ of bulk *SnSe* is lower than that of monolayer *SnSe*. The reason might be that the interactions between layers in bulk *SnSe* leads to smaller group velocity and enhanced scattering of phonons in the in-plane transport, thus result in the lower in-plane κ .

To have a clear overview of the constituent of κ , the frequency dependent κ and average group velocity of monolayer *GeS*, *SnS*, *GeSe*, *SnSe* and bulk *SnSe* along zigzag and armchair directions are plotted in Fig. 5. As shown in Fig. 5(b) and (d), the group velocities of monolayer *SnS* and *SnSe* of the optical phonon branches, especially around middle frequency range (where the phonon dispersion can be separated into two regions with each region containing 6 branches), are very large in a wide range. This is consistent with the phonon dispersions

of monolayer *SnS* and *SnSe* as shown in Fig. 2 that are characterized by markedly dispersive optical phonon branches, which lead to their significant group velocities. From the frequency dependent κ as shown in the top panel, it is obvious that the κ at middle frequency range of monolayer *SnS* and *SnSe* takes up a relatively larger proportion than that of monolayer *GeS* and *GeSe*, which is due to their relatively larger group velocities of the optical phonon modes at middle frequency range. The relaxation time also have some influence on the contributions to κ of phonon branches. For example, as shown in Fig. 4(b), the relaxation time of monolayer *GeS* (black color) at high frequency range above the gap are much smaller than that at low frequency range below the gap. Although monolayer *GeS* have relatively large group velocity at high frequency range, as shown in Fig. 5(a), optical phonon branches above the gap contribute little to κ .

As to bulk *SnSe* (cyan color), as shown in Fig. 4(b), the relaxation time at high frequency range above the gap of bulk *SnSe* are comparable to that at low frequency range below the gap, which is due to the valley of P_3 as shown in Fig. 4(c). Together with its relatively large group velocity at high frequency range, as shown in the insert in Fig. 5(d), optical phonon branches above the gap contribute a lot to κ .

The contributions of different phonon branches (FA, TA, LA and optical) to κ at 300 K are extracted as listed in Table I. The contributions of optical phonon branches increase with the increasing temperature, and at the same time the contributions of acoustic phonon branches decrease. The cumulative κ as a function of the phonon mean free path (MFP) at 300 K for zigzag and armchair directions are fitted to a single parametric function^{34,36}

$$\kappa(l \leq l_{max}) = \frac{\kappa_0}{1 + l_0/l_{max}}, \quad (6)$$

respectively. κ_0 is the ultimate cumulated κ , l_{max} is the maximal MFP concerned, and l_0 is the parameter to be evaluated by fitting. The fitted curves reproduce the calculated data quite well and yield the parameter l_0 for zigzag and armchair directions, respectively, which could be interpreted as the representative MFP (rMFP). The rMFP, as listed in Table I, is helpful for the study of the size effect on the ballistic or diffusive phonon transport, which is important for thermal design with nanostructuring. The rMFP decrease with the increasing temperature due to the integral decrease of MFP and higher contributions to κ coming from optical phonon branches at higher temperature.

Generally speaking, acoustic phonon branches possess larger MFP while optical phonon branches possess smaller MFP, and for acoustic phonon branches lower frequency phonon modes possess larger MFP. Higher contributions of optical phonon branches to κ will lead to smaller rMFP, and higher contributions of acoustic phonon branches to κ , especially from FA, will lead to larger rMFP. It is noticed from Table I that the contributions to κ from optical phonon branches for monolayer *SnS* and *SnSe* are much larger than that for monolayer *GeS* and *GeSe*, and bulk *SnSe* has much larger contributions to κ from optical phonon branches compared with the four monolayer compounds. Thus bulk *SnSe* has the smallest rMFP, and monolayer *SnS* and *SnSe* have smaller rMFP than monolayer *GeS* and *GeSe*. Furthermore, for monolayer *GeSe*, the rMFP along zigzag direction is much smaller than that along armchair direction, while for monolayer *SnS*, the rMFP along zigzag direction is slightly smaller than that along armchair direction. For other monolayer compounds, the rMFP along zigzag direction is larger than that along armchair direction. For monolayer *GeSe*, contributions to κ from FA in zigzag direction is smaller than that in armchair direction while contributions to κ from optical branches in zigzag direction is larger than that in armchair direction.

TABLE II. Elastic constants with unit of kBar.

	GeS	GeSe	SnS	SnSe	bulk SnSe
C_{11}	725.7	677.6	578.6	577.1	691.4
C_{22}	204.1	296.0	272.7	361.7	355.9
C_{33}	-	-	-	-	523.3
C_{44}	283.2	319.7	269.2	286.3	333.0
C_{55}	-	-	-	-	150.6
C_{66}	-	-	-	-	118.2
C_{12}	310.4	299.9	263.9	311.1	313.8
C_{13}	-	-	-	-	97.6
C_{23}	-	-	-	-	132.7

Both factors together result in the much smaller rMFP in zigzag direction than that in armchair direction for monolayer *GeSe*. For monolayer *SnS*, contributions to κ from FA in zigzag direction is smaller than that in armchair direction, and contributions to κ from optical phonon branches in zigzag direction is also smaller than that in armchair direction. The two competing factors result in the slightly smaller rMFP in zigzag direction than that in armchair direction for monolayer *SnS*. For monolayer *GeS*, *SnSe* and bulk *SnSe*, contributions to κ from FA in zigzag direction is larger than that in armchair direction while contributions to κ from optical phonon branches in zigzag direction is smaller than that in armchair direction, which is contrary to the case of monolayer *GeSe*. Both factors together result in the larger rMFP in zigzag direction than that in armchair direction.

VI. ANALYSIS OF THE ANISOTROPY

A. Anisotropy of phonon transport

A distinct feature in Fig. 3 is that, all the four monolayer compounds and bulk *SnSe* possess anisotropic κ . To have a clear comparison of the anisotropy, we plot the κ along zigzag and armchair directions at 300 K for the four monolayer compounds and bulk *SnSe* in Fig. 3(b). It is obvious that the κ of monolayer *GeS* possesses the strongest anisotropy compared to all the other monolayer compounds, and the κ along the zigzag direction of monolayer *GeS* is much larger than others. The κ along zigzag and armchair directions of monolayer *SnSe* shows less anisotropic behavior than that of bulk *SnSe*. The order of anisotropy of the κ of the four monolayer compounds is monolayer *GeS* > *GeSe* > *SnSe* > *SnS*. We further calculated the Young's modulus and found that its order of anisotropy is monolayer *GeS* > *GeSe* > *SnSe* > *SnS*, which is identical with that of κ . The specific values of the Young's modulus of the four monolayer compounds are listed in Table I, and the related elastic constants are shown in Table II.

From Fig. 5, it is clearly shown that the anisotropic behavior of κ is keeping pace with that of group velocity. The frequency dependent κ and average group veloc-

ity are nearly isotropic for high frequency phonon modes above the separatrix frequency (where the gap locates), which separates the phonon dispersion into two regions containing equal numbers of branches. The anisotropy along the two different directions is conspicuous for low frequency phonon modes below the separatrix frequency, which is huge for monolayer *GeS*, small for monolayer *GeSe*, while almost disappear for monolayer *SnS* and *SnSe*. Note that the phonon dispersions of monolayer *GeS* and *GeSe* as shown in Fig. 2 are separated into two regions containing equal numbers of branches with a gap of 2.014 THz and 0.105 THz, respectively, while there is no gap for monolayer *SnS* and *SnSe*. Thus we analyzed that it is the regions below the separatrix frequency where the gap locates that result in the anisotropy. The anisotropy is strong for monolayer *GeS* and weak for monolayer *GeSe* due to the big gap in the phonon dispersions of monolayer *GeS* and the small gap of monolayer *GeSe*. While there is no gap of monolayer *SnS* and *SnSe*, their κ and group velocity along the two different directions are almost isotropic. Thus the anisotropy is associated with the gap of phonon dispersions that the larger the gap the stronger the anisotropy. If we could employ some methods such as strain or doping to modulate the gap, the anisotropy can be effectively modulated, which would be of significance in the thermal management applications. The influence of the gap on the anisotropy can be understood in terms of the coupling between the high and low frequency phonon modes at both sides of the separatrix frequency, which is supported by the scattering channels among phonon modes presented in the next section (Sec. VIB). Since the frequency dependent average group velocity of the four monolayer compounds is nearly isotropic for high frequency phonon modes above the separatrix frequency, the coupling will suppress the anisotropy of the low frequency phonon modes below the separatrix frequency when there is no gap. When a gap exists, the coupling will be weak, leading to the presence of the anisotropy. If the gap is very large, the coupling disappears, resulting in the appearance of the strong anisotropy of low frequency phonon modes.

Based on the analysis demonstrated above, we also would like to present a specific comparison for monolayer *SnSe* and bulk *SnSe*. Monolayer *SnSe* shows less anisotropic properties along zigzag and armchair directions than bulk *SnSe*. There exist some differences between them: 1) The most significant difference is that there is no interactions between layers in monolayer *SnSe*. 2) The difference of lattice constants along the two directions of monolayer *SnSe* is much less than that of bulk *SnSe*, leading to its symmetric square-like lattice structure which determines its almost isotropic properties. 3) The Young's modulus of monolayer *SnSe* is larger than that of bulk *SnSe*, which means that monolayer *SnSe* is more rigid than bulk *SnSe*, leading to the larger group velocity and κ of monolayer *SnSe*. 4) There is no gap in the phonon dispersion of monolayer *SnSe*,

while there is a large gap for bulk *SnSe*. The low and high frequency phonon modes at both sides of the gap are decoupled in bulk *SnSe* due to the large gap, resulting in the huge anisotropy of the group velocity and contributions to κ of low frequency phonon modes below the gap, as shown in the insert of Fig. 5(d). Due to the lack of the gap in the phonon dispersion of monolayer *SnSe*, the coupling between the phonon modes will be very strong, leading to the suppression of the anisotropy.

B. Scattering channel

The phonon scattering channels ruled by the conservation of energy are investigated to quantify the specific scattering processes due to different phonon branches. Since the phonon branches commonly degenerate or cross with each other in the most segments of the path passing through the main high-symmetry k -points in the IBZ as shown in Fig. 2, we only present in Fig. 6 the scattering rate of acoustic phonon modes along Γ -Y direction where the acoustic phonon modes can be easily separated as LA, TA and FA, and the crossover problem is fixed manually. Both the scattering rates for absorption and emission processes as shown in Eq. (4) are addressed and the scattering rates for emission processes are multiplied by 1/2 to avoid counting twice for the same process. To focus on the scattering between acoustic and optical phonon modes, the LA, TA and FA phonon branches are collected together as "A", the 3 low frequency optical phonon branches are collected together as "O1", and the 6 optical phonon branches with high frequency are collected together as "O2". As discussed above, there exists a gap between O1 and O2 for monolayer *GeS* and *GeSe*, while the gap disappears for monolayer *SnS* and *SnSe*.

All the possible phonon scattering channels for the four monolayer compounds are plotted in Fig. 6. Note that the phonon scattering channels are similar for *GeSe*, *SnS* and *SnSe*, while that for *GeS* is different due to the lack of the scattering channels of LA/TA/FA+A/O1 \rightarrow O2, which is resulted from the large gap (2.014 THz) between O1 and O2 for monolayer *GeS*. The major scattering channels that have a large contribution to the overall scattering for monolayer *GeS* are LA/TA/FA+A \rightarrow A, LA/TA/FA \rightarrow A+A and LA+A \rightarrow O1. In contrast, the major scattering channels for monolayer *GeSe*, *SnS* and *SnSe* are LA/TA/FA+A \rightarrow O1. The scattering between A and O1 phonon branches, especially for TA and FA, is highly enhanced due to the tiny or disappeared gap for monolayer *GeSe*, *SnS* and *SnSe*. Furthermore, besides LA/TA/FA+A \rightarrow O1, the scattering channels of TA/FA+O1 \rightarrow O1 for monolayer *SnS*, and the scattering channels of LA/TA/FA+O1 \rightarrow O2, LA+A \rightarrow O2 and TA/FA+O2 \rightarrow O2 for monolayer *SnSe* play a major role. Along with the characteristics of their phonon dispersions as shown in Fig. 2, it can be concluded that a large gap will result in the decoupling between acoustic and high frequency optical phonon modes, and when the gap is

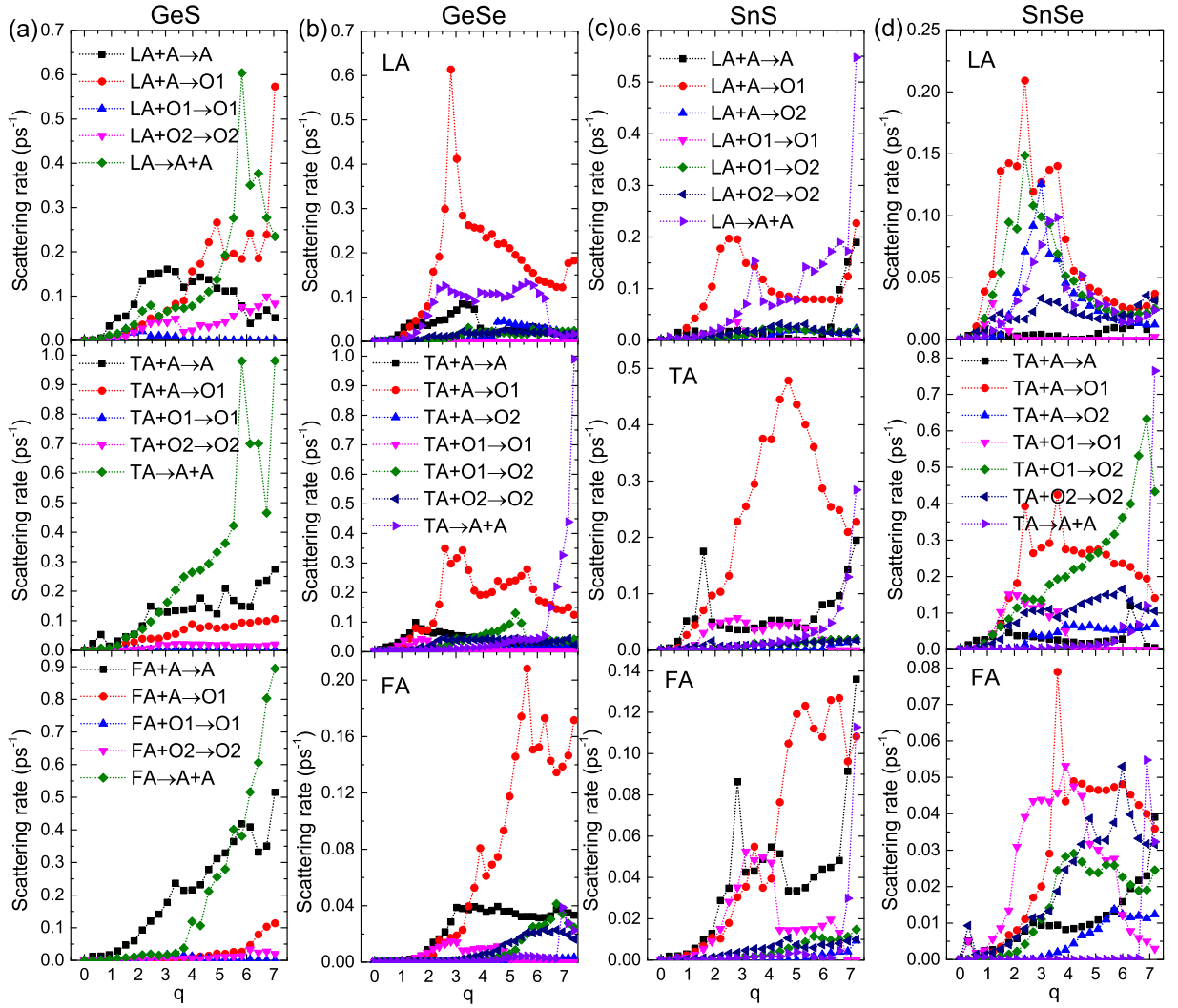


FIG. 6. (Color online) Scattering rate of acoustic phonon modes along Γ -Y direction for monolayer (a) *GeS*, (b) *GeSe*, (c) *SnS* and (d) *SnSe* as labeled on site. The top panel is for LA branch, the middle panel is for TA branch, and the bottom panel is for FA branch. In the legend, "A" means the acoustic phonon branches (LA, TA and FA), "O1" means the 3 optical phonon branches with low frequency, "O2" means the 6 optical phonon branches with high frequency. The legends similar for LA, TA and FA are the same for (b) *GeSe*, (c) *SnS* and (d) *SnSe*, while that for (a) *GeS* is different. The crossover of LA, TA and O1 as shown in Fig. 2 is fixed manually to distinguish them.

tiny or disappears, the phonon branches becomes close to each other, which will result in their strong couplings and lead to a remarkable scattering channel.

It is discussed above based on Fig. 5 that the phonon transport properties of the four monolayer compounds are nearly isotropic for high frequency phonon modes above the separatrix frequency (where the gap locates), which separates the phonon dispersion into two regions containing equal numbers of branches, while the anisotropy along the two different directions is conspicuous for low frequency phonon modes below the separatrix frequency. It is the phonon modes in the region below the separatrix frequency that result in the anisotropy. The coupling between the phonon branches will suppress the anisotropy of the low frequency phonon modes when

there is no gap. When a gap exists, the coupling will be weak, leading to the presence of the anisotropy. If the gap is very large, the coupling disappears, resulting in the appearance of the strong anisotropy of low frequency phonon modes. Thus the anisotropy is huge for monolayer *GeS*, small for monolayer *GeSe*, while almost disappear for monolayer *SnS* and *SnSe*.

C. Electron localization functions

The anisotropic behavior can also be understood from a basic view of the atomic bonding. To picture the electron pair probability, we plot the ELF for the four monolayer compounds in Fig. 7. The ELF contains informa-

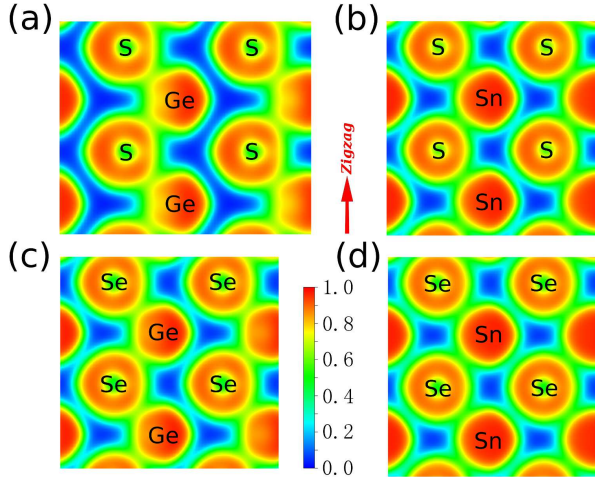


FIG. 7. (Color online) The top view of electron localization functions of monolayer (a) *GeS*, (b) *SnS*, (c) *GeSe* and (d) *SnSe*. The symbols of atoms are marked on site.

tion on the structure of atomic shells, and also displays the location and size of bonding and lone electron pairs.⁴⁸ The ELF characterizes the probability of finding an electron with the same spin in the neighborhood space of the reference electron. The smaller the probability the more localized the reference electron. The ELF is powerful in interpreting chemical bonding patterns, ranging from 0 to 1,⁴⁹ where 0 means no electron, 0.5 corresponds to electron-gas-like pair probability, and 1 corresponds to perfect localization.

As revealed in Fig. 7, the ELF along the zigzag direction for the four monolayer compounds are all larger than 0.5 (the value of uniform electron gas), which means that the electrons are localized. The bonding makes the rigidity along zigzag direction, while for armchair direction, the ELF are all smaller than 0.5, which means that the electrons are delocalized. The ELF along armchair direction is obviously the smallest for monolayer *GeS*, resulting in its softest nature along the armchair direction reflected by its smallest Young's modulus as shown in Table. I. The ELF along the two directions shows a big difference for monolayer *GeS* and *GeSe*, especially for monolayer *GeS*, while shows only a small difference for monolayer *SnS* and *SnSe*. The anisotropic behavior of the ELF reflecting the bonding characteristics is the physical origin of the diverse anisotropic properties for the series of monolayer compounds with hinge-like orthorhombic structure.

VII. SIZE EFFECT

It is well known that, with a larger rMFP, the thermal conductivity could be modulated more effectively by nanostructuring. If the rMFP is very small, the effect of nanostructures with a typical size will be not significant for the phonon transport. As listed in Table I, bulk

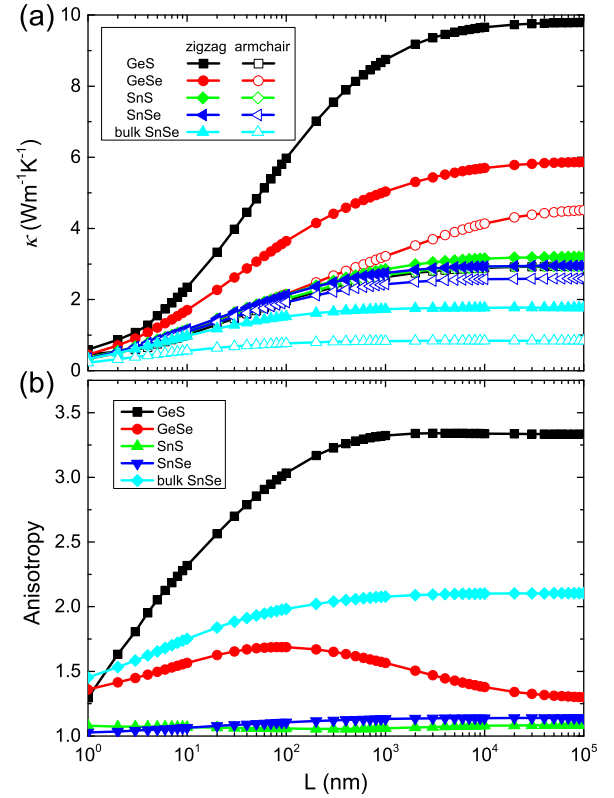


FIG. 8. (Color online) (a) The lattice thermal conductivity (κ) and (b) its anisotropy at 300 K as a function of the system size for completely rough edges. The anisotropy is defined as $\kappa_{\text{zigzag}}/\kappa_{\text{armchair}}$. Points are from calculations and lines are just guide to the eye.

SnSe has the smallest rMFP, and the four monolayer compounds have larger rMFP than bulk *SnSe*, which means that it would be more effective to modulate the phonon transport in the monolayer compounds by nanostructuring. Furthermore, the phonon transport in monolayer *GeS* and *GeSe* could be more effectively modulated due to their larger rMFP compared to that in monolayer *SnS* and *SnSe*. In order to address the size effect on the phonon transport properties, the phonon boundary scattering due to the finite size should be considered, which can be estimated by the standard equation:^{50–52}

$$\frac{1}{\tau_{\lambda}^B} = \frac{1-p}{1+p} \frac{|v_{\lambda}|}{L}, \quad (7)$$

where p is the specularly parameter, which means the fraction of specularly scattered phonons depending on the roughness of the edge, ranging from 0 for a completely rough edge to 1 for a perfectly smooth edge, v_{λ} is the group velocity of the phonon mode λ , and L is the system size usually ranging from nanometers to micrometers. The temperature gradient is assumed to be along the direction of the finite sample length. Anisotropy due to finite sample size is ignored because of the relatively large sizes considered.^{31,53} Then the scattering rate of

each mode is calculated by the Matthiessen rule:

$$\frac{1}{\tau_\lambda} = \frac{1}{\tau_\lambda^{anh}} + \frac{1}{\tau_\lambda^{iso}} + \frac{1}{\tau_\lambda^B}, \quad (8)$$

where $1/\tau_\lambda^{anh}$ is the intrinsic anharmonic scattering rates due to phonon-phonon interactions, and $1/\tau_\lambda^{iso}$ is the scattering rate due to isotopic impurity.

By considering a fully diffusive scattering at the boundary, i.e., $p = 0$, we plot the κ as a function of the system size as shown in Fig. 8(a). When the size is up to near 10^5 nm, the κ for all the monolayer and bulk compounds almost converge to the value of infinite system. The κ decreases with the size decreasing, and the κ along armchair direction of monolayer *GeSe* has the most rapid decrease, which is resulted from its largest rMFP of 72.51 nm. It is obvious that when the size decreases the κ will decrease faster with a larger rMFP. It is also shown that the anisotropy of the κ is affected by the finite size. Generally, the anisotropy will become weak due to the limited size. The reason lies in that usually large κ corresponds to large rMFP and small κ corresponds to small rMFP. Thus the large κ will have a bigger decrease than small κ with limited size, leading to the anisotropy of the κ becoming weak at short length. Based on the κ and rMFP as listed in Table. I, the anisotropy of the κ will become weak for monolayer *GeS*, *SnSe* and bulk *SnSe* with limited size, while the contrary is the case for monolayer *GeSe* and *SnS* that the anisotropy of the κ will become strong with limited size. The cases are confirmed as shown in Fig. 8(b). With limited size, the κ could be effectively lowered and the anisotropy could be effectively modulated by nanostructuring such as patterning into nanoribbon or incorporating pores, which would extend the applications in thermoelectrics and thermal management.

VIII. SUMMARY AND CONCLUSIONS

In summary, we have systematically investigated the diverse phonon transport properties of 2D orthorhombic IV-VI compounds of *GeS*, *GeSe*, *SnS* and *SnSe* by solving the Boltzmann transport equation based on first-principles calculations. They all possess rather low thermal conductivity compared to lots of other 2D materials. The contribution from each phonon branch is studied and its relation with the rMFP is also discussed. The four monolayer compounds, although possessing similar hinge-like structure along the armchair direction as phosphorene, show diverse anisotropic properties in many aspects, such as group velocity, Young's modulus and lattice thermal conductivity (κ), etc. Especially, the κ along the zigzag and armchair directions of monolayer *GeS*

shows the strongest anisotropy while monolayer *SnS* and *SnSe* shows an almost isotropy in phonon transport, despite the similar characteristics of their structures. A detailed analysis on the diverse anisotropic properties of the series 2D orthorhombic compounds is presented. Based on the analysis of the frequency dependent κ and average phonon group velocity, we find that the anisotropy is introduced by the region below the gap between the high frequency optical phonon modes and low frequency phonon modes in the phonon dispersions. The larger the gap, the stronger the anisotropy. The influence of the gap on the anisotropy can be explained from the coupling between the phonon modes at both sides of the gap, which is supported by the phonon scattering channels. The diverse anisotropic behavior can also be understood from a basic view of the atomic bonding characterized by the ELF. The anisotropic behavior of the ELF reflecting the bonding characteristics is the physical origin of the anisotropic properties. We also found that strong anisotropy is associated with weak anharmonic nature. The phonon transport in monolayer *GeS* and *GeSe* can be more effectively modulated by nanostructuring due to their larger rMFP compared to that in monolayer *SnS* and *SnSe*. It is also shown that the anisotropy of the κ is affected by the finite size. With limited size, the κ could be effectively lowered and the anisotropy could be effectively modulated by nanostructuring, which would extend the applications in thermoelectrics and thermal management. This study not only give detailed information of the phonon transport properties of 2D orthorhombic IV-VI compounds of *GeS*, *GeSe*, *SnS* and *SnSe*, but also provide discussions and analysis on the origins of the diverse anisotropy, which would be helpful for further study, modulation and applications of the series of materials with hinge-like orthorhombic structures.

IX. ACKNOWLEDGMENTS

The authors would like to thank Prof. Zhen-Gang Zhu and Prof. Qing-Rong Zheng at UCAS for helpful discussions. G.Q. would like to thank J. Carrete and N. Mingo for providing data of bulk *SnSe*. G.Q. and M.H. acknowledge the support by the Deutsche Forschungsgemeinschaft (DFG) (project number: HU 2269/2-1). This work is supported in part by the NSFC (Grant No. 11004239), the MOST (Grant No. 2012CB932901) of China, and the fund from CAS. The calculations were performed on Nebulae (DAWN6000) in National Supercomputing Center in Shenzhen and MagicCube (DAWN5000A) in Shanghai Supercomputer Center, China, and with computing resources granted by the Jülich Aachen Research Alliance-High Performance Computing (JARA-HPC) from RWTH Aachen University under Project No. jara0132.

- * yan@ucas.ac.cn
† hum@ghi.rwth-aachen.de
‡ gsu@ucas.ac.cn
- ¹ L.-D. Zhao, S.-H. Lo, Y. Zhang, H. Sun, G. Tan, C. Uher, C. Wolverton, V. P. Dravid, and M. G. Kanatzidis, *Nature* **508**, 373 (2014).
 - ² L.-D. Zhao, G. Tan, S. Hao, J. He, Y. Pei, H. Chi, H. Wang, S. Gong, H. Xu, and V. P. Dravid, *Science* **351**, 141 (2016).
 - ³ M. Parenteau and C. Carlone, *Phys. Rev. B* **41**, 5227 (1990).
 - ⁴ R. Guo, X. Wang, Y. Kuang, and B. Huang, *Phys. Rev. B* **92**, 115202 (2015).
 - ⁵ J. Carrete, N. Mingo, and S. Curtarolo, *Appl. Phys. Lett.* **105**, 101907 (2014).
 - ⁶ G. Shi and E. Kioupakis, *J. Appl. Phys.* **117**, 065103 (2015).
 - ⁷ C.-L. Chen, H. Wang, Y.-Y. Chen, T. Day, and G. J. Snyder, *J. Mater. Chem. A* **2**, 11171 (2014).
 - ⁸ Q. Tan, L.-D. Zhao, J.-F. Li, C.-F. Wu, T.-R. Wei, Z.-B. Xing, and M. G. Kanatzidis, *J. Mater. Chem. A* **2**, 17302 (2014).
 - ⁹ H. Zhu, W. Sun, R. Armiento, P. Lazic, and G. Ceder, *Appl. Phys. Lett.* **104**, 082107 (2014).
 - ¹⁰ H. R. Chandrasekhar, R. G. Humphreys, U. Zwick, and M. Cardona, *Phys. Rev. B* **15**, 2177 (1977).
 - ¹¹ T. S. Rao and A. K. Chaudhuri, *J. Phys. D: Appl. Phys.* **18**, L35 (1985).
 - ¹² A. A. Reijnders, J. Hamilton, V. Britto, J.-B. Brubach, P. Roy, Q. D. Gibson, R. J. Cava, and K. S. Burch, *Phys. Rev. B* **90**, 235144 (2014).
 - ¹³ W. J. Baumgardner, J. J. Choi, Y.-F. Lim, and T. Hanrath, *J. Am. Chem. Soc.* **132**, 9519 (2010).
 - ¹⁴ L. C. Gomes and A. Carvalho, *Phys. Rev. B* **92**, 085406 (2015).
 - ¹⁵ J. Vidal, S. Lany, M. dAvezac, A. Zunger, A. Zakutayev, J. Francis, and J. Tate, *Appl. Phys. Lett.* **100**, 032104 (2012).
 - ¹⁶ D. G. Cahill, S. K. Watson, and R. O. Pohl, *Phys. Rev. B* **46**, 6131 (1992).
 - ¹⁷ G. Ding, G. Gao, and K. Yao, *Sci. Rep.* **5**, 9567 (2015).
 - ¹⁸ H. O. H. Churchill and P. Jarillo-Herrero, *Nature Nanotech.* **9**, 330 (2014).
 - ¹⁹ L. Li, Z. Chen, Y. Hu, X. Wang, T. Zhang, W. Chen, and Q. Wang, *J. Am. Chem. Soc.* **135**, 1213 (2013).
 - ²⁰ P. D. Antunez, J. J. Buckley, and R. L. Brutchey, *Nanoscale* **3**, 2399 (2011).
 - ²¹ R. Fei, W. Li, J. Li, and L. Yang, *Appl. Phys. Lett.* **107**, 173104 (2015).
 - ²² G. Ding, G. Gao, *et al.*, arXiv preprint arXiv:1509.01759 (2015).
 - ²³ L.-C. Zhang, G. Qin, W.-Z. Fang, H.-J. Cui, Q.-R. Zheng, Q.-B. Yan, and G. Su, *Sci. Rep.* **6**, 19830 (2016).
 - ²⁴ S. Safaei, M. Galicka, P. Kacman, and R. Buczko, arXiv preprint arXiv:1508.01364 (2015).
 - ²⁵ G. Kresse and D. Joubert, *Phys. Rev. B* **59**, 1758 (1999).
 - ²⁶ G. Kresse and J. Furthmüller, *Phys. Rev. B* **54**, 11169 (1996).
 - ²⁷ J. P. Perdew, K. Burke, and M. Ernzerhof, *Phys. Rev. Lett.* **77**, 3865 (1996).
 - ²⁸ H. J. Monkhorst and J. D. Pack, *Phys. Rev. B* **13**, 5188 (1976).
 - ²⁹ D. A. Broido, M. Malorny, G. Birner, N. Mingo, and D. A. Stewart, *Appl. Phys. Lett.* **91**, 231922 (2007).
 - ³⁰ W. Li, L. Lindsay, D. A. Broido, D. A. Stewart, and N. Mingo, *Phys. Rev. B* **86**, 174307 (2012).
 - ³¹ L. Lindsay, W. Li, J. Carrete, N. Mingo, D. A. Broido, and T. L. Reinecke, *Phys. Rev. B* **89**, 155426 (2014).
 - ³² A. Ward, D. A. Broido, D. A. Stewart, and G. Deinzer, *Phys. Rev. B* **80**, 125203 (2009).
 - ³³ A. Ward and D. A. Broido, *Phys. Rev. B* **81**, 085205 (2010).
 - ³⁴ W. Li, J. Carrete, N. A. Katcho, and N. Mingo, *Comput. Phys. Commun.* **185**, 1747 (2014).
 - ³⁵ G. Qin, Q.-B. Yan, Z. Qin, S.-Y. Yue, H.-J. Cui, Q.-R. Zheng, and G. Su, *Sci. Rep.* **4**, 6946 (2014).
 - ³⁶ G. Qin, Q.-B. Yan, Z. Qin, S.-Y. Yue, M. Hu, and G. Su, *Phys. Chem. Chem. Phys.* **17**, 4854 (2015).
 - ³⁷ M. T. Yin and M. L. Cohen, *Phys. Rev. B* **26**, 3259 (1982).
 - ³⁸ A. Togo, F. Oba, and I. Tanaka, *Phys. Rev. B* **78**, 134106 (2008).
 - ³⁹ L. Lindsay, D. A. Broido, and N. Mingo, *Phys. Rev. B* **82**, 115427 (2010).
 - ⁴⁰ A. H. Castro Neto, F. Guinea, N. M. R. Peres, K. S. Novoselov, and A. K. Geim, *Rev. Mod. Phys.* **81**, 109 (2009).
 - ⁴¹ X. Zhang, H. Xie, M. Hu, H. Bao, S. Yue, G. Qin, and G. Su, *Phys. Rev. B* **89**, 054310 (2014).
 - ⁴² H. Xie, M. Hu, and H. Bao, *Appl. Phys. Lett.* **104**, 131906 (2014).
 - ⁴³ D. Parker and D. J. Singh, *Phys. Rev. B* **82**, 035204 (2010).
 - ⁴⁴ J. J. Pulikkotil, D. J. Singh, S. Auluck, M. Saravanan, D. K. Misra, A. Dhar, and R. C. Budhani, *Phys. Rev. B* **86**, 155204 (2012).
 - ⁴⁵ W. Li, J. Carrete, and N. Mingo, *Appl. Phys. Lett.* **103**, 253103 (2013).
 - ⁴⁶ K. Esfarjani, G. Chen, and H. T. Stokes, *Phys. Rev. B* **84**, 085204 (2011).
 - ⁴⁷ L. Lindsay, D. A. Broido, and T. L. Reinecke, *Phys. Rev. Lett.* **111**, 025901 (2013).
 - ⁴⁸ A. Savin, R. Nesper, S. Wengert, and T. F. Fessler, *Angew. Chem. Int. Ed. Engl.* **36**, 1808 (1997).
 - ⁴⁹ S. N. Steinmann, Y. Mo, and C. Corminboeuf, *Phys. Chem. Chem. Phys.* **13**, 20584 (2011).
 - ⁵⁰ J. Ziman, *Electrons and phonons* (Oxford University Press, London, 1961).
 - ⁵¹ G. P. Srivastava, *The physics of phonons* (CRC Press, 1990).
 - ⁵² D. L. Nika, E. P. Pokatilov, A. S. Askerov, and A. A. Balandin, *Phys. Rev. B* **79**, 155413 (2009).
 - ⁵³ L. Lindsay, D. A. Broido, and N. Mingo, *Phys. Rev. B* **83**, 235428 (2011).